



1 **A global view of the stratospheric background, volcanic and**
2 **wildfire aerosol in the CALIOP era (2006 – 2023)**

3 Bengt G. Martinsson, Johan Friberg, and Moa K. Sporre

4 Department of Physics, Lund University, Lund, Sweden

5 *Correspondence to:* Bengt G. Martinsson (bengt.martinsson@fysik.lu.se)

6 **Abstract.** This study deals with the stratospheric aerosol during the 17 years of lidar
7 measurements with CALIOP. To obtain extinction from the backscattering
8 measurements, we estimated the lidar ratios of the main aerosol injections into the
9 stratosphere. The stratospheric background is estimated by making a subdivision of the
10 stratosphere into nine parts, spanned by three latitude and altitude intervals, reaching
11 background conditions individually at different times. The extracted background shows
12 excellent agreement with solar occultation measurements in the volcanically quiescent
13 period 1998 - 2000. Our results show that 70% of the background aerosol in the deep
14 Brewer-Dobson (dBD) branch is formed above 19 km altitude, indicating strong
15 influence of carbonyl sulfide on the stratospheric background aerosol. The stratosphere
16 was clearly affected by 15 volcanic eruptions and 5 wildfires. Their combined aerosol
17 load affected Southern extratropics, tropics and Northern extratropics almost equally,
18 and the altitude distribution shows that the shallow Brewer-Dobson branch was most
19 affected (43%) followed by the dBD (31%) and lowermost stratosphere (26%). The most
20 important events in order of maximum AOD were the Hunga Ha’apai eruption (2022),
21 Australian wildfires (2019-20) and the eruptions of Raikoke (2019), Sarychev (2009) and
22 Nabro (2011). These events induced strong variability in the stratospheric aerosol
23 optical depth (AOD), causing highly variable climate impact in the period studied with
24 yearly average global effective radiative forcing ranging from -0.14 W/m^2 at background
25 conditions to -0.4 W/m^2 . CALIOP provided important data for stratospheric aerosol
26 climatologies during its 17 years of operation.

27



28 **1. Introduction**

29 Tropospheric air, containing aerosol particles and the sulfurous aerosol precursor gases
30 carbonyl sulfide (OCS) and sulfur dioxide (SO₂), enter the stratosphere across the
31 tropical tropopause. These constituents form the stratospheric background aerosol
32 (Kremser et al., 2016), an aerosol layer above 20 km altitude of water-soluble sulfur-rich
33 particles (Junge et al., 1961). Additional background aerosol originates from the Asian
34 Tropopause Aerosol Layer (ATAL), an aerosol layer between 13 – 18 km altitude over Asia
35 (Vernier et al., 2015). The stratospheric background aerosol contains sulfate, water,
36 organics, and minor traces of tropospheric aerosol and extraterrestrial material
37 (Martinsson et al., 2005; Murphy et al., 2007; Kremser et al., 2016; Martinsson et al.,
38 2019).

39 The stratospheric aerosol load is highly variable due to special aerosol events
40 connected to volcanism (Bauman et al., 2003; Vernier et al., 2009; Solomon et al., 2011;
41 Andersson et al., 2015) and wildfires (Fromm et al., 2010; Martinsson et al., 2022;
42 Friberg et al., 2023), which inject copious amounts of aerosol and precursor gases
43 affecting the stratospheric aerosol for months up to several years (Friberg et al., 2018).
44 These aerosol events induce a variability that needs to be accounted for in climate
45 models. From 1979, the satellite measurement era, the most important volcanic
46 eruptions, El Chichon in 1982 and Mt. Pinatubo (1991), caused a maximum global 3-
47 month average effective radiative forcing of -2 and -3 W/m², respectively (Schmidt et al.,
48 2018). After a period of low volcanic influence on the stratosphere around the turn of
49 the millennium, many volcanic eruptions and wildfires have affected the aerosol in the
50 stratosphere. The most important are the 2019-20 Australian wildfires and the eruptions
51 of Sarychev (2009), Raikoke (2019) and Hunga Ha'apai (2022). The latter had the
52 strongest influence on the stratospheric aerosol, inducing a global 1-year average
53 effective radiative forcing of -0.24 W/m² in addition to the background forcing
54 (Martinsson et al., 2025).

55 Fresh wildfire aerosol particles contain black carbon and a dominating fraction of
56 organics (Garofalo et al., 2019), where the latter is rapidly lost in the stratosphere due to
57 photolysis (Martinsson et al., 2022). The composition of volcanic stratospheric aerosol



58 particles varies. SO₂-rich volcanic emissions, like the 2008 eruption of Kasatochi, are
59 dominated by sulfate, some organics and a minor fraction of ash (Martinsson et al.,
60 2009, Andersson et al., 2013; Friberg et al., 2014). On the other hand, SO₂-poor
61 eruptions, like that of Puyehue-Cordón Caulle in 2011, is dominated by ash (Clarisse et
62 al., 2013). Steam-boosted eruptions of submarine volcanoes (Mastin et al., 2024), like
63 the 2022 eruption of Hunga Ha’apai, can result in a stratospheric aerosol with a strong
64 contribution from sea salt (Martinsson et al., 2025).

65 From the beginning of extensive satellite data in the late 1970s the stratospheric aerosol
66 load has usually been measured using solar occultation (Sato et al., 1993). GloSSAC, a
67 later construction of a continuous record of optical properties of stratospheric aerosol
68 spanning 1979 to present, has a core of solar occultation measurement with the
69 notable 22 year era of SAGE II continuing a few years of solar occultation measurement
70 by SAM II and SAGE I (Thomason et al., 2018). Solar occultation became unavailable
71 during 2005 – 2017. To continue the GloSSAC record, other satellite-based
72 measurements were deployed. The limb scatter instrument OSIRIS (Rieger et al., 2015)
73 and the lidar CALIOP (Cloud-Aerosol Lidar with Orthogonal Polarization) (Winker et al.,
74 2010) were, after substantial recalibration (Thomason et al., 2018, Kovilakam et al.,
75 2020, Kovilakam et al., 2023), used to bridge the gap to obtain continuous time series of
76 stratospheric aerosol properties. Mixing data from many sources that are relying on
77 different measurement principles is however complex, as pointed out by Thomason et
78 al. (2018). We will discuss this matter further in section 4.4.

79 This work deals with the stratospheric aerosol in the CALIOP era, spanning the 17-year
80 period 2006-06-12 to 2023-06-30. CALIOP data (level 1B, version 4-51) is corrected for
81 attenuation, and the lidar ratio is estimated for the stratospheric aerosol resulting from
82 12 volcanic eruptions and wildfires. The stratosphere from the tropopause to 35 km
83 altitude is divided into nine altitude and latitude parts, where the backscattering of the
84 background stratospheric aerosol is identified and its sources discussed. By
85 subtraction of the signal from the background aerosol, the backscattering from major
86 stratospheric aerosol events is obtained. This is converted to AOD using the estimated
87 lidar ratios. We find that the aerosol backscattering on average exceeded the
88 background by 55% in the 17 years studied. The strongest influence from volcanism and



89 wildfires was in 2022 and 2023 due to the submarine Hunga Ha’apai eruption. The
90 second strongest occurred in 2020 due to the Australian wildfires, followed by 2009
91 (Sarychev eruption) and 2019 (Raikoke eruption). 2013 was a year when the entire
92 stratosphere was close to background conditions. Finally, we discuss the validity of lidar
93 data in comparison with the more established data based on solar occultation.

94 **2. Methods**

95 This paper is based on measurements with the CALIOP lidar instrument aboard the
96 CALIPSO (Cloud-Aerosol Lidar and Infrared Pathfinder Satellite Observation) satellite
97 that completed approximately 15 orbits between latitudes -82 and 82° each day.

98 ***2.1 CALIOP properties and methods applied***

99 CALIOP with a laser of 532 nm wavelength produced vertical profiles of backscattering
100 intensity from air molecules, aerosol particles and cloud drops from the ground up to 35
101 km altitude with high vertical resolution depending on altitude. In the altitude ranges <
102 8.2, 8.2 - 20.2, 20.2 – 30.1 and >30.1 km the vertical resolution is 30, 60, 180 and 300 m
103 (Winker et al., 2007, 2010). Here we use data only from the stratosphere, where the
104 tropopause altitude according to MERRA-2 reanalysis (Modern-Era Retrospective
105 analysis for Research and Applications) was used to discriminate data from the
106 troposphere. Only data recorded during nighttime were used in the general evaluation
107 concerning all the CALIOP data available (Friberg et al., 2018; Martinsson et al., 2022).

108 The evaluation is based on version 4-51 of CALIOP level 1B data (NASA/LARC/SD/ASDC,
109 2024). Clouds in the tropopause region were discriminated based on depolarization of
110 the signal, and polar stratospheric clouds were discriminated based on temperature
111 (Friberg et al., 2018; Martinsson et al., 2022). The backscatter data were corrected for
112 attenuation by methodology described in Martinsson et al. (2022) and were first
113 converted to extinction by the standard effective lidar ratio $S = 50 \text{ Sr}$ used for CALIOP
114 (Kar et al., 2019). Volcanic eruptions and wildfires with lidar ratio deviating from 50 Sr by
115 more than 5% were corrected, see sections 2.3 and 4.2.

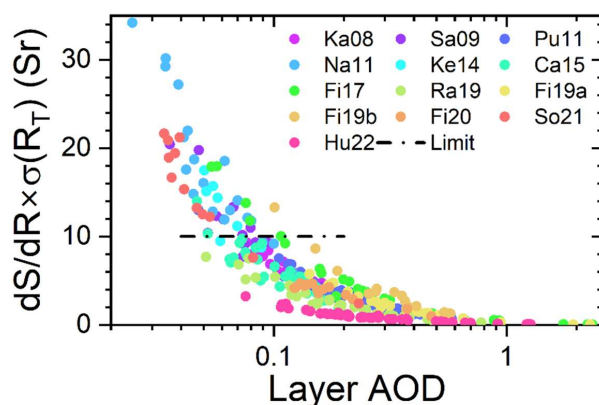
116 ***2.2 Estimation of the stratospheric background***



117 The stratospheric aerosol background can rarely be observed in the entire stratosphere.
118 The last time the stratosphere was practically unaffected by injections from volcanic
119 eruptions and wildfires for several years was a few years around the turn of the
120 millennium (Solomon et al., 2011). Still, we need to find means to estimate the
121 stratospheric background because we can estimate the lidar ratio of stratospheric
122 injections from volcanic eruptions and wildfires (presented in next section) but not for
123 the background aerosol. Injections from aerosol events seldom affect the entire
124 stratosphere. Therefore, parts of the stratosphere can be in background conditions
125 when other parts are affected by aerosol injections.

126 To study the background conditions, the stratosphere was subdivided into nine parts
127 spanned by three altitude layers: the lowermost stratosphere (LMS, from the
128 tropopause to the 380 K isentrope, where the latter was obtained from MERRA-2
129 pressures and temperatures), the shallow Brewer-Dobson branch (sBD, between
130 isentropes 380 and 470 K) and the deep Brewer-Dobson branch (dBD, from the 470 K
131 isentrope to 35 km altitude), and three latitude regions: the Southern extratropics
132 (latitudes -80 to -20°), the tropics (latitudes -20 to 20°) and the Northern extratropics
133 (latitudes 20 to 80°). For each of the 17 years of CALIOP measurements, data were
134 averaged over 8 days resulting in 46 observations per year in each of the nine
135 stratospheric parts. To estimate the background conditions, the averages of the three
136 years with the lowest backscattering measurements of each 8-day period were formed.
137 For two of the nine stratospheric parts, the tropical sBD and dBD, background
138 conditions were rare, wherefore only the two lowest years were used in these two
139 stratospheric parts.

140 The extracted lowest 8-day values formed a seasonal pattern that was fitted by the sum
141 of a constant and a sinusoidal function. These fits were used to express the
142 backscattering of the background aerosol in each of the nine stratospheric parts over
143 the 17 years spanned by CALIOP measurements. The fitted background was subtracted
144 from the measured total backscattering to form the backscattering from volcanic
145 eruptions and wildfires. These background-subtracted backscattering data were
146 converted to AOD via the lidar ratios obtained from individual aerosol events, as
147 described in the next section.



148

149 **Figure 1.** Relation between the layer AOD and the measure on the uncertainty of the
150 lidar ratio estimation. dS/dR is the sensitivity of the lidar ratio (S) to small shifts of the
151 target scattering ratio (R) and $\sigma(R_T)$ is the standard deviation of the target R of each
152 eruption or wildfire obtained beside each aerosol layer investigated. Layers with
153 uncertainty exceeding 10 Sr (“limit”) are discarded in the following analysis.

154 **2.3 Lidar ratio**

155 The lidar ratio of the aerosol from the strongest volcanic eruptions and wildfires in the
156 period studied was estimated based on methodology described in Martinsson et al.
157 (2022), where individual dense aerosol layers are investigated. In that method a target
158 value in scattering ratio (R) obtained beside the studied aerosol layer (R_T) is reached
159 below the layer in an iterative procedure that results in an estimate of the effective lidar
160 ratio, while correcting for attenuation of the backscattered signal.

161 The uncertainty in the estimated lidar ratio depends on the AOD of the layer. A small
162 change in the lidar ratio (S) results in a substantial change in the scattering ratio (R)
163 below a dense layer, i.e., dS/dR is small for dense aerosol layers. dS/dR is obtained by
164 shifting R slightly around R_T . There is also an uncertainty in how well R_T represents the
165 aerosol beneath the layer. We estimate that uncertainty by the standard deviation of the
166 scattering ratio ($\sigma(R_T)$) obtained beside all the aerosol layers studied for each volcanic
167 eruption or wildfire. This is thus based on the assumption that the aerosol beside and
168 below the aerosol layer have the same standard deviation in R , but the actual scattering
169 ratios beside and below an individual layer are uncorrelated. The estimated uncertainty



170 becomes $dS/dR \times \sigma(R_T)$. Figure 1 shows all $dS/dR \times \sigma(R_T)$ related to the AOD of all the
171 estimations of the lidar ratio. The uncertainty in the lidar ratio estimate increases as the
172 layer AOD decreases, hence a limit was set to $dS/dR \times \sigma(R_T) < 10$ Sr to pass as a lidar ratio
173 estimate. As a result, most estimates for three volcanic eruptions, 2011 Nabro (Na11),
174 2014 Kelut (Ke14), and 2021 Soufriere (So21), among the 16 eruptions and wildfires
175 analyzed were lost, as illustrated in Figure 1.

176 For simplicity all the CALIOP data were evaluated using the standard lidar ratio of $S_0 =$
177 50 Sr in the general evaluation. In the study of individual aerosol layers (Figure 1) both
178 the AOD based on the estimated lidar ratio and that based on S_0 were computed, where
179 the latter (AOD_{S_0}) was used to obtain the deviation caused by using S_0 . This deviation
180 depends on the S/S_0 ratio and AOD_{S_0} , where the effect of S/S_0 is the dominant one
181 except for very dense aerosol layers. The result from the general evaluation is corrected
182 afterwards based on the difference between S_0 and the estimated S , see section 4.2.

183 **3. Results**

184 Here we will present the stratospheric aerosol from the troposphere to 35 km altitude
185 and the latitude range -80 to 80° in the era of lidar measurements by the CALIOP
186 instrument aboard the CALIPSO satellite. CALIOP measured the backscattered intensity
187 from a 532 nm laser beam, which can be converted to extinction by multiplying with the
188 ratio of extinction to backscatter, i.e. the lidar ratio. Knowing the lidar ratio thus is
189 central for quantification by obtaining AOD from CALIOP measurements. We developed
190 methodology to estimate the effective lidar ratio from CALIOP measurements, a
191 methodology that also corrects for attenuation of the laser signal (Martinsson et al.,
192 2022). Here we start by presenting the lidar ratio of the main aerosol events of the
193 CALIOP era before giving an overview of the AOD in the period studied.

194 **3.1 Lidar ratio**

195 The main aerosol events affecting the stratosphere in the CALIOP era are presented in
196 Table 1. The methodology we use to estimate lidar ratios requires sufficiently dense
197 aerosol layers as described in section 2, implying that some of the events mentioned in
198 Table 1 are not suitable for the methodology. The lidar ratio was investigated for



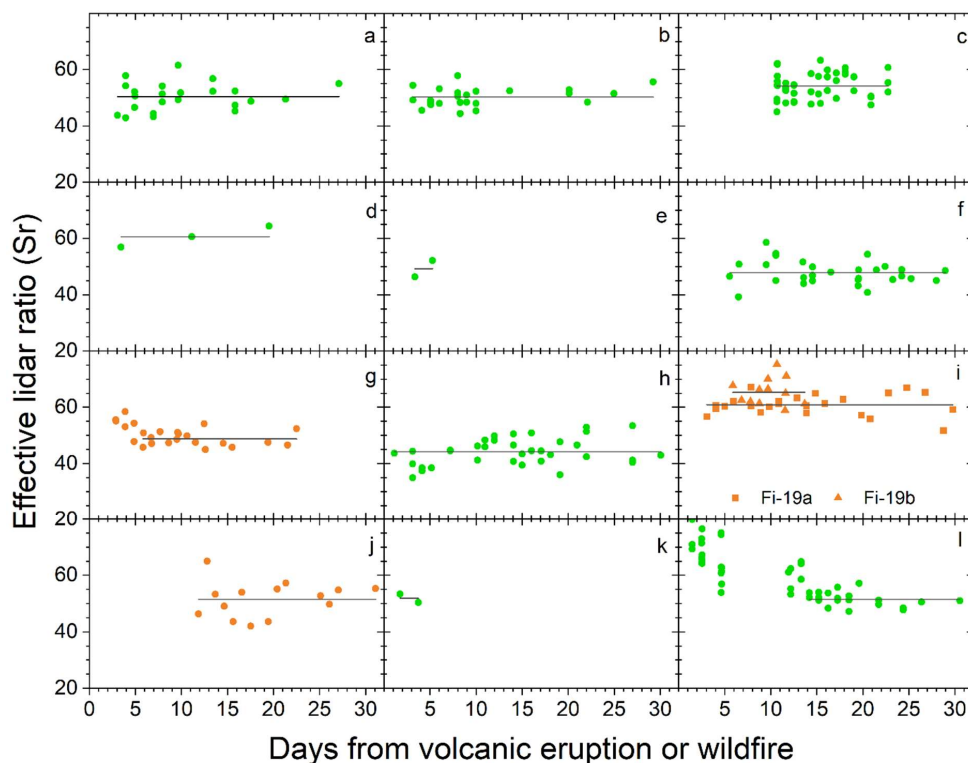
199 **Table 1.** Major volcanic eruptions and wildfires affecting the stratospheric aerosol in the
 200 CALIOP era.

	Date	Volcano/wildfire	Lat ^a	Lon ^b	SO ₂ (Tg)	References
	<i>Volcanic eruptions</i>					
1	2006-05-20	Soufriere Hills (Su)	17°	-62.2°	0.2	Carn and Prata (2010)
2	2006-10-07	Rabaul (Rb)	-4°	152°	0.23	Carn et al. (2009)
3	2008-08-07	Kasatochi (Ka)	52°	-176°	1.7	Thomas et al. (2011)
4	2009-06-12	Sarychev (Sa)	48°	153°	1.2	Haywood et al. (2010)
5	2010-10-05	Merapi (Me)	-7°	110°	0.44	Surono et al. (2012)
6	2011-06-05	Puyehue-Cordón Caulle (Pu)	-40°	-72°	0.25	Clarisse et al. (2012)
7	2011-06-12	Nabro (Na)	13°	42°	1.5	Clarisse et al. (2012)
8	2014-02-13	Kelut (Ke)	-8°	112°	0.18	Li et al. (2017)
9	2015-04-23	Calbuco (Ca)	-41°	-73°	0.3	Pardini et al. (2018)
10	2018-07-27	Ambae (Am)	-15°	168°	0.36	Malinina et al. (2021)
11	2019-06-22	Raikoke (Ra)	48°	153°	1.5	Kloss et al. (2021)
12	2019-06-26	Ulawun (Ul)	-5°	151°	0.14	Kloss et al. (2021)
13	2019-08-03	Ulawun (Ul)	-5°	151°	0.3	Kloss et al. (2021)
14	2021-04-10	Soufriere (So)	13°	-61°	0.31	Taylor et al. (2023)
15	2022-01-15	Hunga Ha'apai (Hu)	-21°	175°	0.45	Carn et al. (2022)
	<i>Wildfires</i>					
16	2006-12-19	Australia (A1)	-37°	147°	-	McCarthy et al. (2012)
17	2009-02-07	Australia (A2)	-38°	146°	-	Cruz et al. (2012)
18	2017-08-12	Canada/USA (CU)	53°	-123°	-	Fromm et al. (2021)
19	2019-12-29	Australia (A3)	-37°	149°	-	Peterson et al. (2021)
20	2020-01-04	Australia (A4)	-37°	149°	-	Peterson et al. (2021)

201

202 stratospheric aerosol from nine volcanic eruptions and three wildfire events (Figure 2).
 203 For some of these aerosol events the screening related to the uncertainty in the
 204 estimated lidar ratio (Figure 1) resulted in few observations, namely for the 2011 Nabro,
 205 2014 Kelut and the 2021 Soufriere eruptions. Most of the eruptions and wildfires display
 206 a stable lidar ratio during the first month, whereas two of the events show an initial
 207 decrease of the lidar ratio, the 2017 North American wildfire (Figure 2g) and the 2022
 208 Hunga Ha'apai eruption (Figure 2l), towards a stable value.

209 Stratospheric aerosol resulting from most of the volcanic eruptions and wildfires has a
 210 lidar ratio close to 50 Sr, which is the commonly used lidar ratio for CALIOP data (Kar et
 211 al., 2019). Notable exceptions with lidar ratio deviating by more than 5% from 50 Sr are
 212 the ash-dominated 2011 eruption of Puyehue-Cordón Caulle (Figure 2c), the 2019



213

214 **Figure 2.** Effective particle lidar ratios the first 30 days after a volcanic eruption or
215 wildfire with a line displaying the average of each event. All measurements concurring
216 with the condition $dS/dR \times \sigma(R) < 10$ are displayed for a) Kasatochi eruption 2008-08-07,
217 b) Sarychev eruption 2009-06-12, c) Puyehue-Cordón-Caulle eruption 2011-06-05, d)
218 Nabro eruption 2011-06-12, e) Kelut eruption 2014-02-13, f) Calbuco eruption 2015-04-
219 23, g) Canada/USA wildfire 2017-08-12, h) Raikoke eruption 2019-06-22, i) Australian
220 wildfire, 2019-12-29 subdivided in part Fi-19a (observations in the vortex (Kablik et al.,
221 2020)) and Fi-19b (observations outside the vortex), j) Australian wildfire 2020-01-04, k)
222 Soufriere eruption 2021-04-10 and l) Hunga Ha'apai eruption 2022-01-15. The averages
223 include all data points except for the Canada/USA wildfire and the Hunga Ha'apai
224 eruption where the initial decline in the lidar ratio is not part of the average represented
225 by horizontal lines.

226

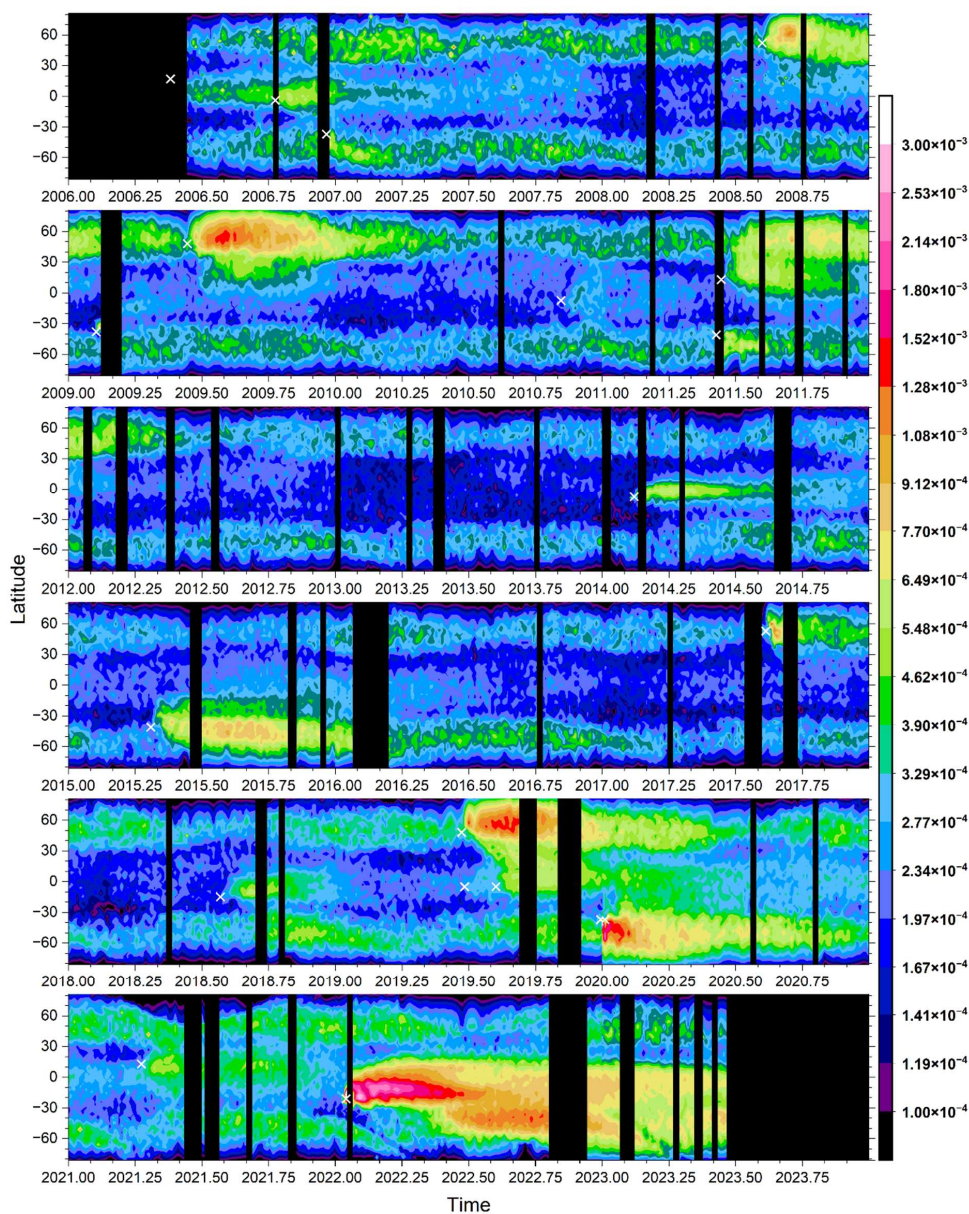


227 Raikoke eruption (Figure 2h) and the Australian wildfire in the last days of 2019 (Figure
228 2i). Also, the 2011 Nabro eruption (Figure 2d) tends to deviate from the commonly
229 adopted lidar ratio of 50 Sr of the stratospheric aerosol, however the observations are
230 too few for a firm conclusion. In the forthcoming presentation the lidar ratio of 50 Sr will
231 be used before a discussion on the influence from deviations is addressed in sections
232 4.2 and 4.3.

233 **3.2 Stratospheric aerosol events overview**

234 At least 15 volcanic eruptions and 5 wildfires clearly affected the stratospheric aerosol
235 in the CALIOP era (Table 1). The latitude distribution of the stratospheric aerosol from
236 the tropopause to 35 km altitude is shown in Figure 3, and subdivided into three layers,
237 dBD, sBD, and LMS, in Figures S1 – S3. Additionally, the altitude distribution is shown in
238 three latitude ranges (Figures S4 – S6).

239 The influence from injections of aerosol from volcanic eruptions and wildfires has
240 durations of a few months to several years (Friberg et al., 2018). The latter category is
241 the aerosol events that enter the dBD branch in the tropics. The outstanding event
242 fulfilling this requirement in the period studied is the submarine eruption of Hunga
243 Ha’apai in 2022 (Figures S1 and S5) where intense volcanism – sea interaction
244 (Seabrook et al., 2023; Mastin et al., 2024) formed large quantities of stratospheric
245 aerosol (Martinsson et al., 2025). The remaining aerosol events in the dBD have much
246 lower AODs. The Kelut eruption in 2014 affected the dBD for approximately 4 years, the
247 combined effect of the 2006 eruptions of Soufriere Hills and Rabaul (Figure S5) show
248 similar long-term effects on the dBD in the tropics (Figure S1). The combined effects of
249 4 volcanic eruptions, the 2018 Ambae, the two 2019 Ulawun and the 2021 Soufriere
250 eruptions, gradually increased the dBD aerosol concentration in the tropics. In addition
251 to these tropical eruptions, some extratropical aerosol events affected the dBD: the
252 2015 Calbuco eruption and some overshooting plumes of the 2019 Raikoke eruption.
253 Three wildfires also contributed aerosol to the extratropical dBD, the 2009 Australian,
254 the 2017 North American and the 2019 Australian wildfires. The aerosol from the latter
255 fire formed a vortex where the aerosol rose above 31 km altitude (Kablick et al., 2020).
256 The extratropical aerosol events leave the dBD faster than the tropical ones because of
257 the extratropical downward motion of the BD circulation.



258

259 **Figure 3.** Aerosol scattering integrated from the tropopause to 35 km altitude averaged
260 over 4 days and 3 degrees in latitude. The lidar ratio is set to 50 Sr. Color scale: Global
261 AOD contribution per degree of latitude, i.e. the sum over latitude is the total AOD at any
262 given time. White crosses indicate time and latitude of aerosol events mentioned in
263 Table 1.

264

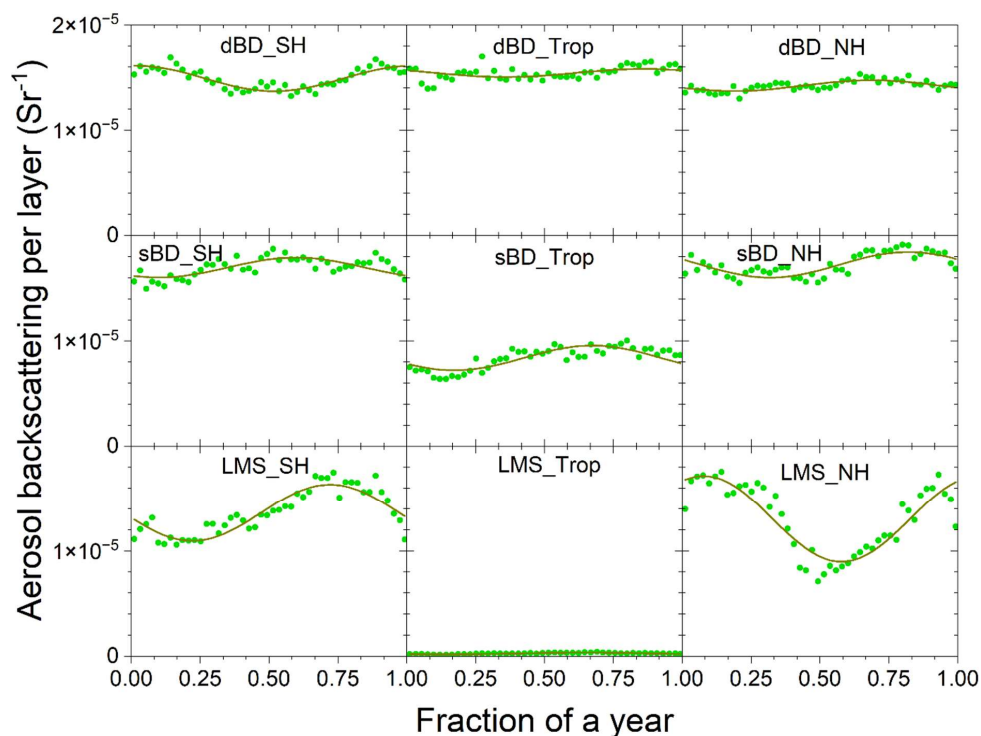


265

266 The shallow Brewer-Dobson (sBD) branch displays no such strong aerosol event as the
267 effect of the 2022 Hunga Ha'apai eruption on the dBD (Figure S2). On the other hand,
268 many events had intermediate or small impacts. The Australian wildfires at the end of
269 2019 and the beginning of 2020 made an initial strong impact that rapidly faded (Friberg
270 et al., 2023), as did the 2017 North American wildfire but with a lower aerosol load
271 (Martinsson et al. 2022) and, to a still lower extent, the 2009 Australian wildfire. The
272 main volcanic eruptions affecting the sBD branch were the 2008 Kasatochi, 2009
273 Sarychev, 2011 Nabro, 2015 Calbuco, 2019 Raikoke and, after a delay due to transport
274 from the dBD branch, the 2022 Hunga Ha'apai eruptions. Other volcanos with smaller
275 impact on the sBD branch were the 2006 Soufriere Hills and Rabaul, the 2010 Merapi,
276 2014 Kelut, 2018 Ambae, 2019 Ulawun (2 eruptions) and 2021 Soufriere eruptions.

277 The LMS, the last stop for air and its trace substances before exiting the stratosphere,
278 are affected by all stratospheric aerosol events. In addition, some extratropical aerosol
279 events do not reach beyond the LMS. The Kasatochi eruption resulted in two distinct
280 aerosol layers, a thin layer in the sBD whereas the main part of its effluents was injected
281 both sides of and close to the tropopause (Andersson et al., 2015). Other exclusive LMS
282 events in the period studied here are the 2011 Puyehue-Cordón Caulle eruption and the
283 2006 Australia wildfire.

284 Most volcanic eruptions show a gradual increase in AOD over few months before
285 reaching its maximum because of the time required to transform sulfur dioxide to
286 sulfate, which usually is the main component of the aerosol from volcanic eruptions.
287 Notable exceptions are the 2022 Hunga Ha'apai and the 2011 Puyehue-Cordón Caulle
288 eruptions (Figure 2). The aerosol of the latter eruption mainly consisted of volcanic ash
289 (Vernier et al., 2013) and the former by aerosol from volcanism – sea interaction
290 (Martinsson et al., 2025). These eruptions are thus less influenced by delay in aerosol
291 formation from chemical transformation. The wildfires in the years 2009, 2017, 2019
292 and 2020 also rapidly reach the maximum AOD before a decline due to photolysis of
293 organic compounds with a half-life of ten days reduces the AOD (Martinsson et al.,
294 2022; Friberg et al., 2023).

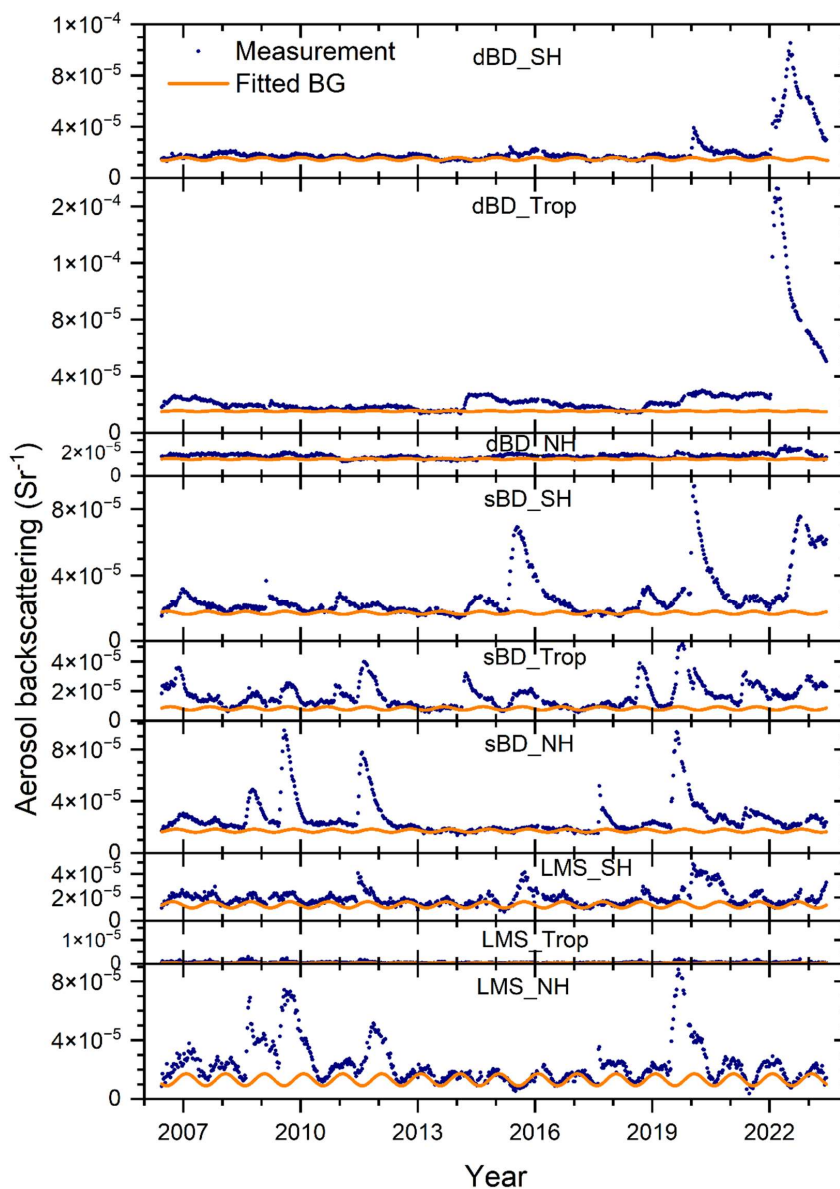


295

296 **Figure 4.** Background aerosol backscattering extracted based on the three lowest
297 average values of each 8-day period over the year in the CALIOP era (2006 – 2023). The
298 extracted data were fitted to a constant and a sinusoidal function. (Exceptions: the two
299 lowest 8-day averages were used for “dBD_Trop” and “sBD_Trop” due to infrequent
300 background values.) The extraction was undertaken in nine regions spanned by
301 latitudes: -80 to -20° (SH), -20 to 20° (Tropics), 20 to 80° (NH) and altitude ranges: the
302 tropopause to 380 K isentrope (LMS), 380 to 470 K isentrope (sBD), 470 K to 35 km
303 altitude (dBD). The data were latitude weighted in the way that the sum of the nine
304 layers is the global aerosol backscattering.

305 4. Discussion

306 We discuss separation of aerosol signals of aerosol events due to volcanic eruptions
307 and wildfires from signals due to stratospheric background aerosol. This is followed by
308 sections on corrections of AOD due to lidar ratio deviations from the commonly
309 assumed 50 Sr. Then we overview the AOD and climate impact and, finally, discuss the
310 validity of AODs from CALIOP relative to solar occultation-based instruments.



311

312 **Figure 5.** Stratospheric aerosol backscattering and fitted background in nine latitude
 313 and altitude regions: the deep BD branch (470 K isentrope to 35 km altitude), the
 314 shallow BD branch (between isentropes 380 and 470 K) and the LMS (from the
 315 tropopause to the 380 K isentrope) and three latitude regions the southern hemisphere
 316 extratropics (-80 to -20°), the tropics (-20 to 20°) and the northern hemisphere
 317 extratropics (20 to 80°) to find time-sections not or weakly affected by stratospheric
 318 aerosol events (see Fig. 4 and text for details).



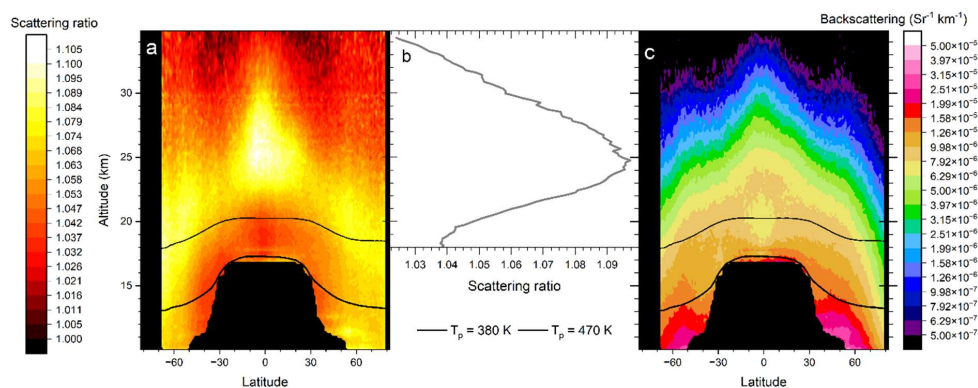
319

320 **4.1 Stratospheric background**

321 The stratospheric background aerosol is not a well-defined concept. One way is to
322 include all but major aerosol events in the background to obtain a persistently variable
323 background (Solomon et al., 2011). An alternative background is based on SAGE II
324 measurements in the volcanically quiescent period in the late 1990s to early 2000s
325 (Kremser et al., 2016). CALIOP measurements were not available in those years. A
326 volcanic eruption or wildfire rarely affects the entire stratosphere. Therefore, we divided
327 the stratosphere into nine sections by altitude and latitude thereby increasing the
328 probability of finding conditions close to background separately in each of the layers
329 using the average of the three lowest backscattering values (in two cases the two
330 lowest) of each layer over the year (Figure 4), as described in the methods section.

331 Seven of the nine layers each contain 11 – 15% of the background aerosol in the
332 stratosphere from the tropopause to 35 km altitude during conditions that are close to
333 background (Table 2). The smallest contribution comes from the tropical LMS, which is
334 to be expected given the small air volume of that layer. The tropical sBD also has a small
335 contribution, but that cannot be explained by the air volume. This layer where
336 tropospheric air enters the stratosphere extends to approximately 20 km altitude, where
337 UV radiation intensity is too weak to efficiently oxidize carbonyl sulfide (Weisenstein et
338 al., 1997), which is an important precursor gas of the stratospheric background aerosol
339 (Crutzen, 1976; Kremser et al., 2016), a topic we return to below. Seasonal changes in
340 aerosol background backscattering are most pronounced in the extratropical LMS,
341 especially in the NH. The volume of LMS varies over the year. That variation
342 (Appenzeller et al., 1996) approximately coincides with the variation in Figure 4 both in
343 terms of seasonality and the stronger amplitude in the LMS of the NH.

344 The backscattering of the stratospheric aerosol and the estimated background (Figure
345 4) in nine altitude and latitude layers is shown in Figure 5. By comparing these two
346 quantities, we verify the underlying assumption in the method used to obtain the
347 background that the stratospheric aerosol background has no long-term trend, which
348 agrees with previous observations (Kremser et al., 2016). Subtracting the background,



349

350 **Figure 6.** The stratospheric aerosol averaged over year 2013, which was close to
351 background conditions. a) The scattering ratio, i.e., the ratio between the total to the
352 modeled backscattering of air molecules. This intensive parameter is not latitude
353 weighted. b) Average scattering ratio in the central tropics (latitudes -10 to 10°)
354 dependence on altitude. c) Aerosol backscattering, this extensive quantity is latitude
355 weighted. Black lines in a) and c) are the yearly average positions of the potential
356 temperatures (T_p) 380 and 470 K.

357

358 we obtain backscattering from volcanic eruptions and wildfires. The net backscattering
359 was converted to AOD of the layers using the lidar ratio of 50 Sr in Figure S7 with
360 contributions from volcanic eruptions and wildfires as described in section 3.2.

361 Except for a tiny peak in the LMS in the Northern extratropics, 2013 is close to
362 background conditions (Figure 5). The stratospheric background aerosol is often
363 thought of as a layer located above 20 km altitude. This is approximately true in terms of
364 scattering ratio (R), the optical equivalent of mixing ratio (Figure 6a). More than half of
365 the air entering the tropical stratosphere is transported polewards in the sBD (Lin and
366 Fu, 2013), where the scattering ratio remains low in a band closest to the tropopause
367 (Figure 6a). This band contains young stratospheric air compared to air at the same
368 altitude but at higher latitude (Austin and Li, 2006; Butchart, 2014; Ploeger et al., 2021).
369 In the air rising further in the tropical stratosphere a dramatic increase of the aerosol
370 mixing ratio can be seen above 20 km altitude. The aerosol signal increases by a factor
371 2.5 (Figure 6b) from 19 to 25 km altitude in the latitude range -10 to 10° , i.e., 70% of the
372 aerosol at 25 km is formed above 19 km altitude. The dBD air is transported polewards
373 and descends at higher latitudes than the sBD air (Figure 6a). With a typical vertical



374 **Table 2.** Average backscattering of background aerosol and AOD of aerosol events in
 375 2006 - 2023 and the distribution over nine stratospheric layers.

Backscattering background ^a				
	<i>Global</i>	SH	Tropics	NH
<i>Total</i>		40%	21%	39%
dBD	39%	13%	14%	12%
sBD	37%	15%	7.3%	15%
LMS	24%	12%	0.2%	11%
AOD aerosol events ^b				
	<i>Global</i>	SH	Tropics	NH
<i>Total</i>		33%	31%	35%
dBD	31%	9.0%	18%	4.0%
sBD	43%	15%	13%	15%
LMS	26%	9.0%	0.4%	17%

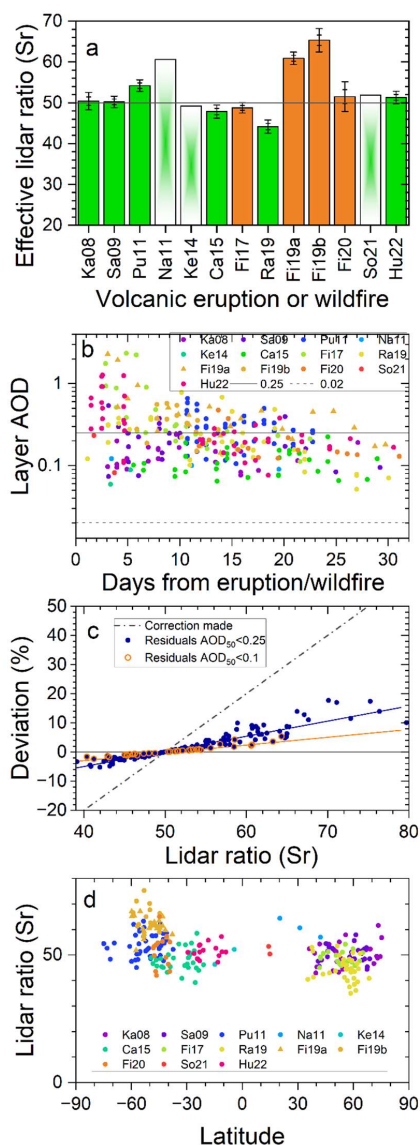
376 ^aAverage backscattering of background = 0.0011 Sr⁻¹

377 ^bAverage AOD from aerosol events (2006 – 2023) = 0.0031

378

379 velocity of 20 m/day (Mote et al., 1998) the transport from the tropical tropopause (at 17
 380 km) to 19 km altitude requires the order 100 days, providing ample time for conversion
 381 of SO₂ before reaching the latter altitude (Nicknish et al., 2025). Hence, little SO₂ enters
 382 the dBD, implying particle formation from another source. Intensifying UV radiation with
 383 altitude causes oxidation of the most abundant sulfur compound in the atmosphere,
 384 i.e., carbonyl sulfide (OCS) (Crutzen, 1976; Kremser et al., 2016), whereas this
 385 compound remains intact in the sBD. The requirement of intense UV radiation for
 386 oxidation makes OCS an important aerosol formation pathway mainly in the dBD. The
 387 formed aerosol is transported polewards where downward transport brings the aerosol
 388 to the sBD and LMS layers before the transport out of the stratosphere (Figure 6a). The
 389 formation pathways of the stratospheric background aerosol are still debated. The
 390 estimated contribution of OCS to the stratospheric background aerosol ranges from 20
 391 – 50% (Sheng et al., 2015; Chin and Davies, 1995) to 70% or more (Crutzen, 1976; Brühl
 392 et al., 2012). High-resolution lidar data, like that of CALIOP, can be used to constrain
 393 modeling efforts to understand the sources of the background aerosol.

394 When instead considering the absolute background aerosol load (Figure 6c) we find the
 395 highest aerosol load at low stratospheric altitudes. The air in the Brewer-Dobson



396

397 **Figure 7.** a) Average lidar ratios according to Fig. 2 with standard errors and 95% ranges
 398 of volcanic eruptions and wildfires. Too few observations for error estimations were
 399 obtained for the eruptions of Nabro (Na11), Kelut (Ke14) and Soufriere (So21). b) AODs
 400 of aerosol layers with $dS/dR \times \sigma(R) < 10$ Sr Vs. time from the eruption or wildfire. The full
 401 line illustrates approximate maximum layer AOD after 1 month, and the broken line
 402 indicates the approximate maximum layer AOD observable by limb-viewing techniques
 403 (note: logarithmic y-scale). c) Correction of AOD obtained by setting the lidar ratio to 50
 404 Sr (AOD_{50}), based on a linear dependence of the AOD on the lidar ratio. The residual
 405 deviation after the correction of two categories is also shown: aerosol layers with AOD_{50}
 406 < 0.1 and < 0.25 . d) Estimated lidar ratios in Figure 2 Vs. latitude.



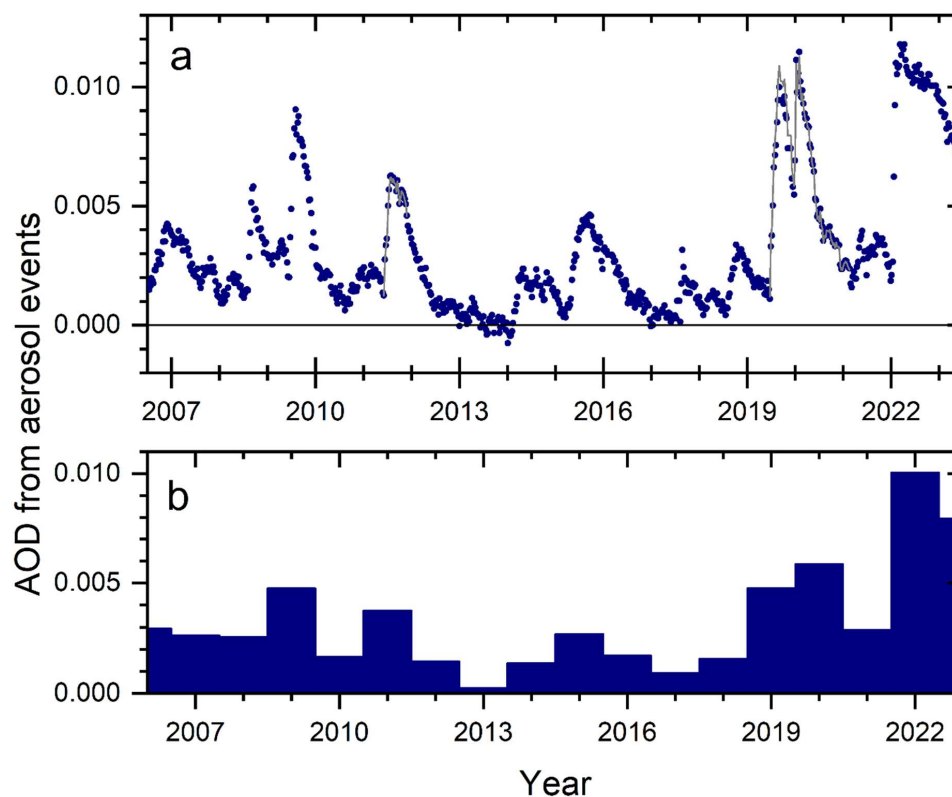
407 circulation becomes compressed during the downwelling in the extratropics. During
408 background conditions approximately 60% of the aerosol backscattering signal is found
409 in the two lower layers, sBD and LMS (Table 2), containing aerosol transported from
410 both the sBD and dBD of the tropics.

411 **4.2 Correction of lidar ratio**

412 This far we have presented AODs with the lidar ratio set to 50 Sr. The lidar ratios of the
413 individual measurements are shown in Figure 2. In Figure 7a we show the averages with
414 statistical uncertainty (standard error and double-sided 95% confidence interval). As
415 already pointed out, three of the eruptions (Nabro 2011, Kelut 2014 and Soufriere 2021)
416 cannot be evaluated statistically due to few available measurements. Most of the
417 aerosol events show lidar ratios of approximately 50 Sr, whereas the aerosol from
418 Puyehue-Cordón Caulle (2011), Raikoke (2019) and the Australian wildfires in the end of
419 2019 deviates from 50 Sr by more than 5%.

420 To convert the AOD obtained using $S_0 = 50$ Sr to the estimated lidar ratio (S) we need to
421 consider the linear dependence of the AOD on the lidar ratio. A secondary effect relates
422 to the level of AOD. For the latter, we need to evaluate the occurrence of dense aerosol
423 layers. All the measurements fulfilling the criteria on uncertainty of the lidar ratio
424 estimate (Figure 1) are displayed in Figure 7b. Initially layer AODs sometimes exceed 1.
425 After 20 days the AOD of the individual aerosol layers is mostly 0.25 and lower, except
426 for the 2019 Australian wildfire that remain somewhat higher probably due to less air
427 mixing in the vortex formed (Kablick et al., 2020). We corrected the AODs by S/S_0 for
428 volcanic eruptions and wildfires that formed an aerosol with effective lidar ratio
429 deviating more than 5% from $S_0 = 50$ Sr, whereas the residual correction connected with
430 the AOD of an aerosol layer was not accounted for (see the methods section for further
431 detail) because the effect is small (Figure 7c). In the general evaluation we did not
432 separate the aerosol backscattering from the 2019 and 2020 Australian wildfires that
433 were only a few days apart. The 2020 fire was dominant in terms of AOD with 80 – 90%
434 of the total AOD from the two fires (Friberg et al., 2023). Here, we weigh the lidar ratios
435 of the two fires accordingly to obtain $S = 53.3$ representing both fires.

436



437

438 **Figure 8.** Background-subtracted AOD of the stratosphere from the tropopause to 35
439 km altitude and averaged from -80 to 80° in latitude. a) AOD from main stratospheric
440 aerosol events caused by volcanic eruptions and wildfires. AOD₅₀ is shown (full grey
441 line) where correction due to lidar ratio deviating from 50 Sr^{-1} is undertaken (Pu11, Ra19
442 and Fi19&20). b) Yearly averages of data in a). Note that the horizontal tick marks
443 indicate start of a year in a) and the middle of a year in b). Also note that the averages of
444 years 2006 and 2023 span only half years due to the mid-year start (2006) and finish
445 (2023) of the CALIOP measurements.

446

447 The blue dots in Figure 8a over the stratospheric AOD were corrected for deviant lidar
448 ratios in 2011 (Puyehue-Cordón Caulle eruption) and 2019 – 2020 (Raikoke eruption and
449 Australian wildfires). The corresponding AOD using $S_0 = 50 \text{ Sr}$ is represented by a thin
450 gray line showing that the AOD was practically not affected by the correction in 2011
451 because that year was dominated by aerosol from another eruption (Nabro, Figure 3).
452 The AOD from the Raikoke (2019) eruption shifted down slightly by the correction, and



453 that of the 2019 – 2020 Australian wildfires was shifted upwards. Altogether the change
454 in AOD from the corrections due to deviant lidar ratio were minor.

455 **4.3 AOD of stratospheric aerosol events**

456 The AOD from aerosol events were approximately evenly distributed over the three
457 latitude regions (SH, Tropics and NH) studied (Table 2). The altitude distribution showed
458 most influence from volcanic eruptions and wildfires in the sBD (43%), followed by the
459 dBD (31%), and the often overlooked LMS (Andersson et al., 2015) held 26% of the AOD
460 from aerosol events in the period 2006 – 2023.

461 The average stratospheric AOD, with the contribution from background aerosol
462 subtracted, from the tropopause to 35 km altitude in the latitude range -80 to 80° is
463 shown in Figure 8a. The intense volcanism – sea interaction of the Hunga Ha’apai
464 eruption in the beginning of 2022 (Martinsson et al., 2025) resulted in the highest and
465 broadest AOD peak (Figure 8a). Other prominent events were the Australian wildfires at
466 the end of 2019 and the beginning of 2020, the eruptions of Raikoke (2019), Sarychev
467 (2009), Nabro (2011), Calbuco (2015) and Kasatochi (2008) affecting the stratospheric
468 AOD together with several eruptions and wildfires having smaller contributions (Table
469 1).

470 The average influence of volcanic eruptions and wildfires each year is shown in Figure
471 8b. The most affected year was 2022 with an average AOD of 0.01 from aerosol events.
472 That year is likely followed by 2023, for which we have no data from the second half of
473 the year. Both these years were mainly affected by the 2022 Hunga Ha’apai eruption.
474 Then follows 2020 (mainly the 2019-20 Australian wildfires with some contribution from
475 the Raikoke eruption) with background-subtracted AOD of 0.06, 2009 (Sarychev) and
476 2019 (Raikoke) both years with event AOD of 0.05, whereas 2011 (mainly Nabro) reach
477 AOD from aerosol events of almost 0.04. The average background-subtracted AOD from
478 volcanic eruptions and wildfires from 2006 to 2023 is 0.0031. The background aerosol
479 produces backscattering of 0.0011 Sr^{-1} , which, with the unverified assumption of a lidar
480 ratio of 50 Sr, corresponds to a stratospheric background AOD of 0.0057.

481 The yearly average AOD from aerosol events ranges from 0.0002 (in 2013) to 0.010
482 (2022), resulting in a variability range of 0.010 around the average of 0.0031. Making use



483 of previous estimates of the relation between radiative forcing and stratospheric AOD
484 (Schmidt et al., 2018), the global stratospheric yearly average total effective radiative
485 forcing due to volcanic eruptions and wildfires varies between -0.006 and -0.24 W/m^2 ,
486 with the average -0.074 W/m^2 in the period 2006 to 2023. Assuming a lidar ratio of 50 Sr,
487 the stratospheric background aerosol effective radiative forcing becomes -0.14 W/m^2 .

488 **4.4 The validity of AODs from CALIOP**

489 Stratospheric aerosol optical properties are often described using solar occultation
490 data, especially from the 22 years of SAGE II measurements (Bauman et al., 2003;
491 Thomason et al., 2018). Comparisons of CALIOP lidar-based results with solar
492 occultation (SAGE III/ISS) show discrepancy at mid- and high latitudes (Kar et al., 2019)
493 and at low altitudes (Kovilakam et al., 2023). The main reason for these differences was
494 attributed to the unknown lidar ratio of CALIOP (Kar et al., 2019; Kovilakam et al., 2023).
495 Here we have estimated the CALIOP lidar ratio of the aerosol from several volcanic
496 eruptions and wildfires (Figure 2), and in Figure 7d the latitude distribution of the
497 estimates is shown. Using the standard lidar ratio of 50 Sr cannot explain the latitude-
498 and altitude-dependence claimed in Kar et al. (2019) and Kovilakam et al. (2023) for
499 aerosol from volcanic eruptions and wildfires in the CALIOP era.

500 The latitude-dependent discrepancy between SAGE III/ISS and CALIOP at high altitudes
501 in the period June 2017 to August 2018 above 20 km (, i.e., essentially in the dBD)
502 reported by Kar et al. (2019) concerns a period when the dBD was close to background
503 (Figure 5). The method used here for estimating the lidar ratio does not work for
504 background conditions (Figure 1). Using 50 Sr for background aerosol results in the
505 global average background AOD of 0.0057. SAGE II measurements during the
506 volcanically quiescent period 1998 – 2000 resulted in AOD of 0.0040 (estimated from
507 Solomon et al. (2011), their Figure 2), who integrated the stratospheric AOD from 15 km
508 altitude. When removing the stratospheric aerosol data below 15 km from the CALIOP
509 measurements, the stratospheric background AOD is reduced by 31% to 0.0039 using
510 lidar ratio 50 Sr. This is almost identical to the background AOD reported in Solomon et
511 al. (2011), thus indicating that the stratospheric background aerosol on average has a
512 lidar ratio close to 50 Sr. Kar et al. (2019) found that backscattering during background
513 conditions at altitudes above 20 km in the extratropics should be converted by a



514 variable lidar ratio. In Figure 6c we find most of the aerosol above 20 km altitude in the
515 tropics, implying that the deviations at high latitudes according to Kar et al. (2019) have
516 little impact on global AOD, and thus the comparison dealing with the entire
517 stratosphere above 15 km altitude.

518 In a comparison by Kovilakam et al. (2023) between CALIOP and SAGE III/ISS during
519 November 2017, 2 – 3 months after the Canada/USA fire (Table 1) similar deviations
520 were found at high altitudes as in Kar et al. (2019), as described above. That comparison
521 also found large differences in the densest part of the stratosphere at altitudes below 17
522 km, where clouds frequently interfere with limb-viewing measurements. In GloSSAC the
523 more than 50% lower values of limb-viewing techniques (SAGE and OSIRIS) than
524 CALIOP were implemented citing uncertainties in the lidar ratio to discard CALIOP
525 results at low altitudes (Kovilakam et al., 2023).

526 The main advantages of solar occultation measurements are that extinction is
527 measured and that several wavelengths are available. With known lidar ratio, lidar
528 measurements with nadir view have some distinct advantages compared to solar
529 occultation limb views. First of all, lidars have several hundred kilometers shorter
530 measurement path enabling measurements in dense aerosol layers (Martinsson et al.,
531 2022, their Figure 7) providing viable, quantitative results when limb views fail.

532 Secondly, the lidar vertical resolution is superior and is not relying on assumptions on
533 homogeneity of the aerosol layer measured, like solar occultation measurements do
534 (Damadeo et al., 2013). Accurate altitude descriptions with high vertical resolution of
535 stratospheric injections (Sandvik et al., 2021) is vital for the outcome of stratospheric
536 aerosol modeling (Axebrink et al., 2025). With these clear advantages we argue that
537 lidar measurements should be given a more prominent role in stratospheric aerosol
538 climatologies presented to the modeling community than in the present version of
539 GloSSAC (Thomason et al., 2018, Kovilakam et al., 2020; Kovilakam et al., 2023).

540 Hopefully the lidar ratio of stratospheric aerosol can be further clarified when the
541 aerosol load is close to background conditions by lidar systems measuring both
542 backscattering and extinction. The ATLID aboard the EarthCARE satellite (Illingworth et
543 al., 2015) that started to produce data in July 2024 and the NASA and Italian Space
544 Agency collaboration on the 3 wavelength lidar CALIGOLA planned for launch in the



545 early 2030s (Behrenfeld et al., 2023) are future means to further clarify extinction
546 obtained from lidars, and to optimally combine solar occultation and lidar
547 measurements for future long-term records on the optical properties of the
548 stratospheric aerosol with high and unambiguous vertical resolution.

549 **5. Conclusions**

550 The entire backscattering record at 532 nm wavelength of the satellite-based lidar
551 system CALIOP spanning years 2006 to 2023 was investigated in this study. During this
552 period injections of aerosol and precursor gases into the stratosphere of 15 volcanic
553 eruptions and 5 wildfires were identified. The lidar ratios of 12 volcanic eruptions and
554 wildfires were investigated to convert the measured backscattering to extinction. The
555 measurements were evaluated and corrected for attenuation using the lidar ratio $S_0 = 50$
556 Sr. The aerosol events having a lidar ratio deviating by more than 5% from S_0 were
557 corrected after the general evaluation.

558 Background conditions are more probable in sublayers than in the entire stratosphere.
559 The stratosphere was subdivided into 9 layers spanned by altitude (lowermost
560 stratosphere (LMS), shallow Brewer-Dobson branch (sBD), deep Brewer-Dobson branch
561 (dBD)) and latitude intervals (tropics and Southern and Northern extratropics). The
562 backgrounds of layers were combined to obtain that of the entire stratosphere. The
563 backscattering of background aerosol was converted to aerosol optical depth (AOD)
564 using a lidar ratio of 50 Sr. That AOD agrees well with measurements with solar
565 occultation (SAGE II) during 1998 – 2000 in the volcanically quiescent period. Seven of
566 the nine layers each contain 11- 15% of the entire background aerosol. The tropical LMS
567 has a small contribution due to very small volume compared to the other layers. The
568 tropical sBD was also clearly lower (7%) because oxidation of carbonyl sulfide (OCS)
569 occurs at higher altitudes in the upwards moving air in the tropical stratosphere. We find
570 that 70% of the aerosol in the tropical dBD is formed above 19 km altitude during
571 background conditions, due to formation from OCS. Poleward followed by downward
572 transport of the dBD aerosol to the sBD and LMS takes place at mid and high latitudes,
573 whereas the tropical sBD air is transported polewards in a band close to the tropopause
574 ending up in the LMS at lower latitudes than the dBD air. Considering the ongoing



575 debate on the sources of stratospheric background aerosol, these highly resolved
576 CALIOP data could be useful to constrain modeling efforts on the subject.

577 The background aerosol was subtracted from the measurements to obtain the influence
578 from aerosol and trace gas injections into the stratosphere. The most important aerosol
579 events in the 17-year period are the 2022 Hunga Ha'apai eruption and the Australian
580 wildfires (2019-20) followed by the volcanic eruptions Raikoke (2019), Sarychev (2009)
581 and Nabro (2011). With the background AOD (0.0057) subtracted, the yearly average
582 AOD spans 0 to 0.010. The yearly average radiative forcing of the background-
583 subtracted aerosol is estimated to be in the range -0.006 (year 2013) to -0.24 W/m²
584 (2022).

585 Limb-viewing solar occultation measurements have some distinctive advantages in that
586 much of the early measurements in the satellite era were undertaken with that method.
587 They also deliver direct measurements of extinction, and at several wavelengths. Here,
588 we have estimated the lidar ratio of the CALIOP measurements to obtain extinction from
589 backscattering measurements. Lidars operating in nadir view, like CALIOP, have several
590 hundred kilometers (or a factor of more than 100) shorter measurement path than limb-
591 viewers, allowing measurements in dense aerosol layers where limb-viewers fail. Lidars
592 have unambiguous and superior vertical resolution over other satellite instruments
593 providing models with important input data of aerosol and trace gas injections into the
594 stratosphere. Newer lidars that measure extinction are launched, under construction
595 and planned. Now is the time to better sort out differences between lidars and solar
596 occultation measurements, especially in the dense stratospheric air located below 17
597 km altitude in records over the optical properties of the stratospheric aerosol.

598 **References**

- 599 Andersson, S. M., Martinsson, B. G., Friberg, J., Brenninkmeijer, C. A. M., Rauthe-
600 Schöch, A., Hermann, M., van Velthoven, P. F. J., and Zahn, A.: Composition and
601 evolution of volcanic aerosol from eruptions of Kasatochi, Sarychev and
602 Eyjafjallajökull in 2008–2010 based on CARIBIC observations, *At mos. Chem.*
603 *Phys.*, 13, 1781–1796, <https://doi.org/10.5194/acp-13-1781-2013>, 2013.
- 604 Andersson, S. M., Martinsson, B. G., Vernier, J.-P., Friberg, J., Brenninkmeijer, C. A. M.,
605 Hermann, M., van Velthoven, P. F. J., and Zahn, A.: Significant radiative impact of



- 606 volcanic aerosol in the lowermost stratosphere, *Nat. Commun.*, 6, 1–8,
607 <https://doi.org/10.1038/ncomms8692>, 2015.
- 608 Appenzeller, C., Holton, J.R., and Rosenlov, K.H.: Seasonal variation of mass transport
609 across the tropopause, *J. Geophys. Res.* 101, 15071-15078, 1996.
- 610 Austin, J., and Li, F.: On the relationship between the strength of the Brewer-Dobson
611 circulation and the age of stratospheric air, *Geophys. Res. Lett.*, 33, L17807,
612 [doi:10.1029/2006GL026867](https://doi.org/10.1029/2006GL026867), 2006.
- 613 Axebrink, E., Sporre, M.K., and Friberg, J.: Impact of SO₂ injection profiles on simulated
614 volcanic forcing for the 2009 Sarychev eruptions– investigating the importance of
615 using high-vertical-resolution methods when compiling SO₂ data, *Atmos. Chem.*
616 *Phys.*, 25, 2047–2059, <https://doi.org/10.5194/acp-25-2047-2025>, 2025.
- 617 Bauman, J. J., Russell, P. B., Geller, M. A., and Hamill, P.: A stratospheric aerosol
618 climatology from SAGE II and CLAES measurements: 2. Results and
619 comparisons, 1984–1999, *J. Geophys. Res.*, 108, 4383,
620 <https://doi.org/10.1029/2002JD002993>, 2003.
- 621 Behrenfeld, M.J., Lorenzoni, L., Hu, Y., Bissom, K.M., Hostetler, C.A., Di Girolamo, P.,
622 Dionisi, D., Longo, F., and Zoffoli, S.: Satellite Lidar Measurements as a Critical
623 New Global Ocean Climate Record, *Remote Sens.* 15, 5567. [https://doi.org/](https://doi.org/10.3390/rs15235567)
624 [10.3390/rs15235567](https://doi.org/10.3390/rs15235567), 2023.
- 625 Brühl, C., Lelieveld, J., Crutzen, P.J., and Tost, H.: The role of carbonyl sulphide as a
626 source of stratospheric sulphate aerosol and its impact on climate, *Atmos.*
627 *Chem. Phys.*, 12, 1239–1253, www.atmos-chem-phys.net/12/1239/2012/
628 [doi:10.5194/acp-12-1239-2012](https://doi.org/10.5194/acp-12-1239-2012), 2012.
- 629 Butchart, N., The Brewer-Dobson circulation, *Rev. Geophys.*, 52, 157–184,
630 [doi:10.1002/2013RG000448](https://doi.org/10.1002/2013RG000448), 2014.
- 631 Carn, S.A., Krueger, A.J., Krotkov, N.A., Yang, K., and Evans, K.: Tracking volcanic sulfur
632 dioxide clouds for aviation hazard mitigation, *Nat Hazards*, 51, 325–343 DOI
633 [10.1007/s11069-008-9228-4](https://doi.org/10.1007/s11069-008-9228-4), 2009.
- 634 Carn, S.A., and Prata, F.J., Satellite-based constraints on explosive SO₂ release from
635 Soufrière Hills Volcano, Montserrat, *Geophys. Res. Lett.*, 37, 1-5, L00E22,
636 [doi:10.1029/2010GL044971](https://doi.org/10.1029/2010GL044971), 2010.
- 637 Carn, S. A., Krotkov, N. A., Fisher, B. L., and Li, C.: Out of the blue: Volcanic SO₂
638 emissions during the 2021–2022 eruptions of Hunga Tonga– Hunga Ha’apai
639 (Tonga), *Front. Earth Sci.*, 10, 976962,
640 <https://doi.org/10.3389/feart.2022.976962>, 2022.
- 641 Chin, M., and Davies, D.D.: A reanalysis of carbonyl sulfide as a source of stratospheric
642 background sulfur aerosol, *J. Geophys. Res.* 100, 8993-9005, 1995.



- 643 Clarisse, L., Hurtmans, D., Clerbaux, C., Hadji-Lazaro, J., Ngadi, Y., and Coheur, P.-F.:
644 Retrieval of sulphur dioxide from the infrared atmospheric sounding
645 interferometer (IASI), *Atmos. Meas. Tech.*, 5, 581–594,
646 <https://doi.org/10.5194/amt-5-581-2012>, 2012.
- 647 Clarisse, L., Coheur, P.-F., Prata F., Hadji-Lazaro, J., Hurtmans, D., and Clerbaux, C.: A
648 unified approach to infrared aerosol remote sensing and type specification,
649 *Atmos. Chem. Phys.*, 13, 2195–2221, www.atmos-chem-phys.net/13/2195/2013/
650 doi:10.5194/acp-13-2195-2013, 2013.
- 651 Crutzen, P.J.: The possible importance of CSO for the sulfate layer of the stratosphere,
652 *Geophys. Res. Lett.* 3, 73-76, 1976.
- 653 Cruz, M.G., Sullivan, A.L., Gould, J.S., Sims, N.C., Bannister, A.J., Hollis, J.J., and Hurley,
654 R.J.: Anatomy of a catastrophic wildfire: The Black Saturday Kilmore East fire in
655 Victoria, Australia, *Forest Ecol. Manag.* 284, 269-295, 2012.
- 656 Damadeo, R.P., Zawodny, J.M., Thomason, L.W., and Iyer, N.: SAGE version 7.0
657 algorithm: application to SAGE II, *Atmos. Meas. Tech.*, 6, 3539–3561,
658 www.atmos-meas-tech.net/6/3539/2013/, 2013.
- 659 Friberg, J., Martinsson, B. G., Andersson, S. M., Brenninkmeijer, C. A. M., Hermann, M.,
660 Van Velthoven, P. F. J., and Zahn, A.: Sources of increase in lowermost
661 stratospheric sulphurous and carbonaceous aerosol background concentrations
662 during 1999–2008 derived from CARIBIC flights, *Tellus B*, 66, 23428,
663 <https://doi.org/10.3402/tellusb.v66.23428>, 2014.
- 664 Friberg, J., Martinsson, B. G., Andersson, S. M., and Sandvik, O. S.: Volcanic impact on
665 the climate– the stratospheric aerosol load in the period 2006–2015, *Atmos.*
666 *Chem. Phys.*, 18, 11149–11169, <https://doi.org/10.5194/acp-18-11149-2018>,
667 2018.
- 668 Friberg, J., Martinsson, B. G., and Sporre, M. K.: Short- and long-term stratospheric
669 impact of smoke from the 2019–2020 Australian wildfires, *Atmos. Chem. Phys.*,
670 23, 12557–12570, <https://doi.org/10.5194/acp-23-12557-2023>, 2023.
- 671 Fromm, M., Lindsey, D. T., Servranckx, R., Yue, G., Trickl, T., Sica, R., Doucet, P., and
672 Godin-Beekmann, S.: The untold story of pyrocumulonimbus, *B. Am. Meteorol.*
673 *Soc.*, 91, 1193–1209, 2010.
- 674 Fromm, M., Kablick III, G. P., Peterson, D. A., Kahn, R. A., Flower, V. J. B., and Sefor, C. J.:
675 Quantifying the source term and uniqueness of the August 12, 2017 Pacific
676 Northwest pyroCb event, *J. Geophys. Res.*, 126, e2021JD034928,
677 <https://doi.org/10.1029/2021JD034928>, 2021.
- 678 Garofalo, L. A., Levin, E. J. T., Campos, T., Kreidenweis, S. N., and Farmer, D. K.:
679 Emission and evolution of submicron organic aerosol in smoke from wild fires in
680 the western United States, *ACS Space Chem.*, 3, 1237–1247, 2019.



- 681 Haywood, J.M., Jones, A., Clarisse, L., Bourassa, A., Barnes, J., Telford, P., Bellouin, N.,
682 Boucher, O., Agnew, P., Clerbaux, C., Coheur, P., Degenstein, D., and Braesicke,
683 P.: Observations of the eruption of the Sarychev volcano and simulations using
684 the HadGEM2 climate model, *J. Geophys. Res.*, 115, D21212,
685 doi:10.1029/2010JD014447, 2010.
- 686 Illingworth, A. J., Barker, H. W., Beljaars, A., Ceccaldi, M., Chepfer, H., Clerbaux, N.,
687 Cole, J., Delanoë, J., Domenech, C., Donovan, D. P., Fukuda, S., Hirakata, M.,
688 Hogan, R. J., Huenerbein, A., Kollias, P., Kubota, T., Nakajima, T., Nakajima, T. Y.,
689 Nishizawa, T., Ohno, Y., Okamoto, H., Oki, R., Sato, K., Satoh, M., Shephard, M.
690 W., Velázquez-Blázquez, A., Wandinger, U., Wehr, T., and van Zadelhoff, G.-J.: The
691 Earth CARE Satellite: The Next Step Forward in Global Measurements of Clouds,
692 Aerosols, Precipitation, and Radiation, *B. Am. Meteorol. Soc.*, 96, 1311–1332,
693 <https://doi.org/10.1175/BAMS-D-12-00227.1>, 2015.
- 694 Junge, C.E., Chagnon, C.W., and Manson, J.E.: A World-wide Stratospheric Aerosol
695 Layer, *Science*, 133, 1478-1479, 1961.
- 696 Kablick, G. P., Allen, D. R., Fromm, M. D., and Nedoluha, G. E.: Australian PyroCb Smoke
697 Generates Synoptic-Scale Stratospheric Anticyclones, *Geophys. Res. Lett.*, 47,
698 e2020GL08810, <https://doi.org/10.1029/2020GL088101>, 2020.
- 699 Kar, J., Lee, K.-P., Vaughan, M. A., Tackett, J. L., Trepte, C. R., Winker, D. M., Lucker, P. L.,
700 and Getzewich, B. J.: CALIPSO level 3 stratospheric aerosol profile product:
701 version 1.00 algorithm description and initial assessment, *Atmos. Meas. Tech.*,
702 12, 6173–6191, <https://doi.org/10.5194/amt-12-6173-2019>, 2019.
- 703 Kloss, C., Berthet, G., Sellitto, P., Ploeger, F., Taha, G., Tidiga, M., Eremenko, M.,
704 Bossolasco, A., Jégou, F., Renard, J.-B., and Legras, B.: Stratospheric aerosol
705 layer perturbation caused by the 2019 Raikoke and Ulawun eruptions and their
706 radiative forcing, *Atmos. Chem. Phys.*, 21, 535–560, <https://doi.org/10.5194/acp-21-535-2021>, 2021.
- 708 Kovilakam, M., Thomason, L.W., Ernest, N., Rieger, L.A., Bourassa, A.E., and Millán, L.:
709 The Global Space-based Stratospheric Aerosol Climatology (version 2.0): 1979–
710 2018, *Earth Syst. Sci. Data*, 12, 2607–2634, <https://doi.org/10.5194/essd-12-2607-2020>, 2020.
- 712 Kovilakam, M., Thomason, L.W., and Knepp, T.: SAGEIII/ISS aerosol/cloud categorization
713 and its impact on GloSSAC, *Atmos. Meas. Tech.*, 16, 2709–2731,
714 <https://doi.org/10.5194/amt-16-2709-2023>, 2023.
- 715 Kremser, S., Thomason, L. W., von Hobe, M., Hermann, M., Deshler, T., Timmreck, C.,
716 Toohey, M., Stenke, A., Schwarz, J. P., Weigel, R., Fueglistaler, S., Prata, F. J.,
717 Vernier, J. P., Schlager, H., Barnes, J. E., Antuña-Marrero, J. C., Fairlie, D., Palm,
718 M., Mahieu, E., Notholt, J., Rex, M., Bingen, C., Vanhellefont, F., Bourassa, A.,
719 Plane, J. M. C., Klocke, D., Carn, S. A., Clarisse, L., Trickl, T., Neely, R., James, A.
720 D., Rieger, L., Wilson, J. C., and Meland, B.: Stratospheric aerosol– Observations,



- 721 processes, and impact on climate, *Rev. Geophys.*, 54, 278–335,
722 <https://doi.org/10.1002/2015RG000511>, 2016.
- 723 Li, C., Krotkov, N.A., Carn, S., Zhang, Y., Spurr, R.D.J., and Joiner, J.: New-generation
724 NASA Aura Ozone Monitoring Instrument (OMI) volcanic SO₂ dataset: algorithm
725 description, initial results, and continuation with the Suomi-NPP Ozone Mapping
726 and Profiler Suite (OMPS), *Atmos. Meas. Tech.*, 10, 445–458, [www.atmos-meas-](http://www.atmos-meas-tech.net/10/445/2017/)
727 [tech.net/10/445/2017/](http://www.atmos-meas-tech.net/10/445/2017/), doi:10.5194/amt-10-445-2017, 2017.
- 728 Lin, P., and Fu, Q., Changes in various branches of the Brewer–Dobson circulation from
729 an ensemble of chemistry climate models, *J. Geophys. Res.*, 118, 73–84,
730 doi:10.1029/2012JD018813, 2013.
- 731 Malinina, E., Rozanov, A., Niemayer, U., Wallis, S., Arosio, C., Wrana, F., Timmreck, C.,
732 von Savigny, C., and Burrows, J.P.: Changes in stratospheric aerosol extinction
733 coefficient after the 2018 Ambae eruption as seen by OMPS-LP and MAECHAM5-
734 HAM, *Atmos. Chem. Phys.*, 21, 14871–14891, [https://doi.org/10.5194/acp-21-](https://doi.org/10.5194/acp-21-14871-2021)
735 [14871-2021](https://doi.org/10.5194/acp-21-14871-2021), 2021.
- 736 Martinsson, B. G., Nguyen, H. N., Brenninkmeijer, C. A. M., Zahn, A., Heintzenberg, J.,
737 Hermann, M., and Velthoven, P. F. J. v.: Characteristics and origin of lowermost
738 stratospheric aerosol at northern midlatitudes under volcanically quiescent
739 conditions based on CARIBIC observations, *J. Geophys. Res.*, 110, D12201,
740 doi:10.1029/2004JD005644, 2005.
- 741 Martinsson, B. G., Brenninkmeijer, C. A. M., Cam, S. A., Hermann, M., Heue, K.P., van
742 Velthoven, P. F. J., and Zahn, A.: Influence of the 2008 Kasatochi volcanic
743 eruption on sulfurous and carbonaceous aerosol constituents in the lower
744 stratosphere, *Geophys. Res. Lett.*, 36, 1–5,
745 <https://doi.org/10.1029/2009GL038735>, 2009.
- 746 Martinsson, B. G., Friberg, J., Sandvik, O. S., Hermann, M., van Velthoven, P. F. J., and
747 Zahn, A.: Formation and composition of the UTLS aerosol, *npj Climate and*
748 *Atmospheric Science*, 2, 1–6, <https://doi.org/10.1038/s41612-019-0097-1>, 2019.
- 749 Martinsson, B. G., Friberg, J., Sandvik, O. S., and Sporre, M. K.: Five-satellite-sensor
750 study of the rapid decline of wildfire smoke in the stratosphere, *Atmos. Chem.*
751 *Phys.*, 22, 3967–3984, <https://doi.org/10.5194/acp-22-3967-2022>, 2022.
- 752 Martinsson, B. G., Friberg, J., and Sporre, M. K.: Stratospheric aerosol formed by intense
753 volcanism–sea interaction during the 2022 Hunga Ha’apai eruption, *Atmos.*
754 *Chem. Phys.*, 25, 10677–10690, <https://doi.org/10.5194/acp-25-10677-2025>,
755 2025.
- 756 Mastin, L. G., Van Eaton, A. R., and Cronin, S. J.: Did steam boost the height and growth
757 rate of the giant Hunga eruption plume?, *B. Volcanol.*, 86, 64,
758 <https://doi.org/10.1007/s00445-024-01749-1>, 2024.



- 759 McCarthy, G.J., Plucinski, M.P., and Gould, J.S.: Analysis of the resourcing and
760 containment of multiple remote fires: The Great Divide Complex of fires, Victoria,
761 December 2006, *Australian Forestry*, 75, 54-63, DOI:
762 10.1080/00049158.2012.10676385, 2012.
- 763 Mote, P.W., Dunkerton, T.J., McIntyre, M.E., Ray, E.A., Haynes, P.H., and Russell III, J.M.:
764 Vertical velocity, vertical diffusion, and dilution by midlatitude air in the tropical
765 lower stratosphere, *J. Geophys. Res.* 103, 8651-8666, 1998.
- 766 Murphy, D. M., Cziczo, D. J., Hudson, P. K., and Thomson, D. S.: Carbonaceous material
767 in aerosol particles in the lower stratosphere and tropopause region, *J. Geophys.*
768 *Res.*, 112, D04203, <https://doi.org/10.1029/2006JD007297>, 2007.
- 769 NASA/LARC/SD/ASDC: Science CALIPSO Lidar Level 1B profile data, V4-51, NASA
770 Langley Atmospheric Data Center DAAC,
771 https://doi.org/10.5067/CALIOP/CALIPSO/CAL_LID_L1_Standard-V4-51, 2024.
- 772 Nicknish, P.A., Stone, K., Solomon, S., and Carn, S.A.: Quantifying the decay timescale
773 of volcanic sulfur dioxide in the stratosphere, *Atmos. Chem. Phys.*, 25, 11535–
774 11555, <https://doi.org/10.5194/acp-25-11535-2025>, 2025.
- 775 Pardini, F., Burton, M., Arzilli, F., La Spina, G., and Polacci, M.: SO₂ emissions, plume
776 heights and magmatic processes inferred from satellite data: The 2015 Calbuco
777 eruptions, *J. Volcanol. Geotherm. Res.* 361, 12-24, 2018.
- 778 Peterson, D. A., Fromm, M. D., McRae, R. H. D., Campbell, J. R., Hyer, E. J., Taha, G.,
779 Camacho, C. P., Kablick, G. P., Schmidt, C. C., and DeLand, M. T.: Australia's
780 Black Summer pyrocumulonimbus super outbreak reveals potential for
781 increasingly extreme stratospheric smoke events, *Npj Clim. Atmos. Sci.*, 4, 38
782 <https://doi.org/10.1038/s41612-021-00192-9>, 2021.
- 783 Ploeger, F., Diallo, M., Charlesworth, E., Konopka, P., Legras, B., Laube, J.C., Gross, J.-U.,
784 Günther, G., Engel, A., and Riese, M.: The stratospheric Brewer–Dobson
785 circulation inferred from age of air in the ERA5 reanalysis, *Atmos. Chem. Phys.*,
786 21, 8393–8412, <https://doi.org/10.5194/acp-21-8393-2021>, 2021.
- 787 Rieger, L.A., Bourassa, A.E., and Degenstein, D.A.: Merging the OSIRIS and SAGE II
788 stratospheric aerosol records, *J. Geophys. Res. Atmos.*, 120, 8890–8904,
789 doi:10.1002/2015JD023133, 2015.
- 790 Sandvik, O. S., Friberg, J., Sporre, M. K., and Martinsson, B. G.: Methodology to obtain
791 highly resolved SO₂ vertical profiles for representation of volcanic emissions in
792 climate models, *Atmos. Meas. Tech.*, 14, 7153–7165,
793 <https://doi.org/10.5194/amt-14-7153-2021>, 2021.
- 794 Sato, M., Hansen, J.E., McCormick, M.P., and Pollack J.B.: Stratospheric aerosol optical
795 depths, 1850-1990, *J. Geophys. Res.* 98, 22987-22994, 1993.



- 796 Schmidt, A., Mills, M. J., Ghan, S., Gregory, J. M., Allan, R. P., Andrews, T., Bardeen, C. G.,
797 Conley, A., Forster, P. M., Gettelman, A., Portmann, R. W., Solomon, S., and Toon,
798 O. B.: Volcanic radiative forcing from 1979 to 2015, *J. Geophys. Res.-Atmos.*, 123,
799 12491–12508, <https://doi.org/10.1029/2018JD028776>, 2018.
- 800 Seabrook, S., Mackay, K., Watson, S. J., Clare, M. A., Hunt, J. E., Yeo, I. A., Lane, E. M.,
801 Clark, M. R., Wysoczanski, R., Rowden, A.A., Kula, T., Hoffmann, L.J., Armstrong,
802 E., and Williams, M. J. M.: Volcaniclastic density currents explain widespread
803 and diverse seafloor impacts of the 2022 Hunga Volcano eruption, *Nat.*
804 *Commun.*, 14, 7881, <https://doi.org/10.1038/s41467-023-43607-2>, 2023.
- 805 Sheng, J.-X., Weisenstein, D.K., Luo, B.-P., Rozanov, E., Stenke, A., Anet, J., Bingemer, H.,
806 and Peter, T.: Global atmospheric sulfur budget under volcanically quiescent
807 conditions: Aerosol-chemistry-climate model predictions and validation, *J.*
808 *Geophys. Res. Atmos.*, 120, 256–276, doi:10.1002/2014JD021985, 2015.
- 809 Solomon, S., Daniel, J. S., Neely, R. R., Vernier, J.-P., Dutton, E. G., and Thomason, L. W.:
810 The persistently variable “background” stratospheric aerosol layer and global
811 climate change, *Science*, 333, 866–870, 2011.
- 812 Surano, Jousset, P., Pallister, J., Boichu, M., Boungiorno, M.F., Budisantoso, A., Costa, F.,
813 Andreastuti, S., Prata, F., Schneider, D., Clarisse, L., Humaida, H., Sumarti, S.,
814 Bignami, C., Griswold, J., Carn, S., Oppenheimer C., and Lavigne F.: The 2010
815 explosive eruption of Java's Merapi volcano—A ‘100-year’ event, *J. Volcanol.*
816 *Geotherm. Res.* 241-242, 121-135, 2012.
- 817 Taylor, I. A., Grainger, R. G., Prata, A. T., Proud, S. R., Mather, T. A., and Pyle, D. M.: A
818 satellite chronology of plumes from the April 2021 eruption of La Soufrière, St
819 Vincent, *Atmos. Chem. Phys.*, 23, 15209–15234, [https://doi.org/10.5194/acp-23-](https://doi.org/10.5194/acp-23-15209-2023)
820 [15209-2023](https://doi.org/10.5194/acp-23-15209-2023), 2023.
- 821 Thomas, H.E., Watson, I.M., Carn, S.A., Prata, A.J., and Realmuta, V.J.: A comparison of
822 AIRS, MODIS and OMI sulphur dioxide retrievals in volcanic clouds, *Geomatics,*
823 *Natural Hazards and Risk*, 2, 217-232, 2011.
- 824 Thomason, L.W., Ernest, N., Millán, L., Rieger, L., Bourassa, A., Vernier, J.-P., Manney, G.,
825 Luo, B., Arfeuille, F., and Peter, T.: A global space-based stratospheric aerosol
826 climatology: 1979-2016, *Earth Syst. Sci. Data*, 10, 469–492,
827 <https://doi.org/10.5194/essd-10-469-2018>, 2018.
- 828 Vernier, J.-P., Pommereau, J.P., Garnier, A., Pelon, J., Larsen, N., Nielsen, J.,
829 Christiansen, T., Cairo, F., Thomason, L.W., Leblanc, T., and McDermid, I.S.:
830 Tropical stratospheric aerosol layer from CALIPSO lidar observations, *J.*
831 *Geophys. Res.*, 114, D00H10, doi:10.1029/2009JD011946, 2009.
- 832 Vernier, J.-P., Farlie, T.D., Murray, J.J., Tupper, A., Trepte, C., Winker, D., Pelon, J., Garnier,
833 A., Jumelet, J., Pavolonis, M., Omar, A.H., and Powell, K.A.: An Advanced System



- 834 to Monitor the 3D Structure of Diffuse Volcanic Ash Clouds *J. Appl. Meteorol.*
835 *Clim.* 10, 2125-2138, 2013.
- 836 Vernier, J.-P., Farlie, T.D., Natarajan, M., Wiengold, F.G., Bian, J., Martinsson, B.G.,
837 Crumeyrolle, S., Thomason, L.W., and Bedka, K.M.: Increase in upper
838 tropospheric and lower stratospheric aerosol levels and its potential connection
839 with Asian pollution, *J. Geophys. Res.*, 120, doi:10.1002/2014JD022372, 2015.
- 840 Weisenstein, D.K., Yue, G.K., Ko, M.K.W., Sze, N.-D., Rodriguez, J.M., and Scott, C.J.: A
841 two-dimensional model of sulfur species and aerosol, *J. Geophys. Res.* 102,
842 13019-13035, 1997.
- 843 Winker, D. M., Hunt, W. H., and McGill, M. J.: Initial performance assessment of CALIOP,
844 *Geophys. Res. Lett.*, 34, 1–5, <https://doi.org/10.1029/2007GL030135>, 2007.
- 845 Winker, D. M., Pelon, J., Coakley, J. A., Ackerman, S. A., Charlson, R. J., Colarco, P. R.,
846 Flamant, P., Fu, Q., Hoff, R. M., Kittaka, C., Kubar, T. L., Le Treut, H., McCormick,
847 M. P., Mégie, G., Poole, L., Powell, K., Trepte, K., Vaughan, M. A., and Wielicki, B.
848 A.: The CALIPSO mission— A global 3D view of aerosols and clouds, *B. Am.*
849 *Meteorol. Soc.*, 91, 1211–1229, <https://doi.org/10.1175/2010BAMS3009.1>, 2010.
- 850 *Data availability.* The data used are publicly available: CALIOP V4.51 lidar data
851 (<https://search.earthdata.nasa.gov/search?fp=CALIPSO>).
- 852 *Author contributions.* BGM planned the study, undertook most of the data analysis and
853 wrote the paper. JF participated in the planning of the study, undertook part of the data
854 analysis and MKS contributed. JF and MKS undertook data extraction and handling for
855 the data analysis. All authors participated in discussions and commented on the
856 manuscript.
- 857 *Disclaimer.* The contact author and the co-authors declare that they have no competing
858 interests.
- 859 *Acknowledgements.* Aerosol products from the CALIOP sensor were produced by NASA
860 Langley Research Center.
- 861 *Financial support.* The Swedish National Space Agency, contracts 2025-00200 and
862 2022-00157, Johan Friberg. The Crafoord Foundation, contract 20240901, Johan Friberg.
863 Formas, contract 2020-00997, Moa Sporre. The Swedish Research Council 2022-02836,
864 Moa Sporre.